Tuning pharmaceutically active zein-based formulations for additive manufacturing

Mélanie Thadasack, Anne-Laure Réguerre, Eric Leroy, Sofiane Guessasma, Denis Lourdin, Timm Weitkamp, Laurent Chaunier

Tuning pharmaceutically active zein-based formulations for additive manufacturing

Mélanie Thadasack[a], Anne-Laure Réguerre[a], Eric Leroy[b], Sofiane Guessasma[a], Denis Lourdin[a], Timm Weitkamp[c] and Laurent Chaunier[a*]

[*]Corresponding author: laurent.chaunier@inrae.fr

[a]INRAE, UR BIA, F-44316, Nantes

[b]Université de Nantes, Oniris, CNRS, GEPEA, UMR 6144, F-44600 Saint Nazaire

[c]Synchrotron SOLEIL, F-91190 Saint-Aubin

Abstract

Zein, a biopolymer from corn, was plasticized by glycerol and an Active Pharmaceutical Ingredient-Ionic Liquid (API-IL) for its melt processing at 130 °C. In order to enhance the rheological properties of the formulation for 3D printing, the ratio of glycerol to API-IL was adjusted while maintaining a consistent addition of 20% plasticizer. A 50/50 ratio allowed obtaining an initial melt viscosity suitable for extrusion-based processes, at approximately 1 kPa.s at a shear rate of 10 s^{-1}, with a shear thinning behavior. This viscosity remained stable during a processing window of about 6 min, before zein proteins start to aggregate, leading to an apparent gelation phenomenon for long residence times. The processability of this formulation containing API-IL for the printing of tablets for potential therapeutic applications was confirmed by tests on a 3D printer. Nonetheless, in comparison to a reference formulation containing only glycerol, the printing accuracy experienced a decrease. This was ascribed to slower viscous sintering kinetics in presence of API-IL, evidenced by monitoring fusion-bonding during dynamic X-ray tomography trials carried out at synchrotron SOLEIL.

Keywords

Hot Melt Extrusion; Processing window; Protein; In-situ synchrotron micro-CT; Sintering

1. Introduction

The advent of Additive Manufacturing processes is a great opportunity for personalized medicine. In particular, edible 3D printed objects containing active ingredients with customized porous structures may allow their controlled release *in vivo* [1-3]. Among the numerous existing technologies, those based on extrusion of thermoplastic formulations, allow obtaining high quality structures faithful to their initial numerical models, thanks to fast stiffening of deposited layers upon cooling [4-7]. However, they require optimized formulations combining edible thermoplastic biopolymer matrices with active ingredients, matching both processing specifications and therapeutic end-uses, *i.e.* passive diffusion of active molecules [8,9]. The time and temperature processing window of such formulations must be tuned taking into consideration the thermo-sensitivity of active ingredients, the rheology of the matrix in the molten state, and the impact of the hot melt extrusion process on the material, especially when shaping pharmaceutical tablets [10, 11].

Zein, a protein extracted from corn, can be formulated with plasticizers for hot melt extrusion [12, 13]. Indeed, materials based on zein plasticized by 20w% glycerol show a rheological behavior at 130 °C that is similar to that of standard polymers used in additive manufacturing such as PLA and ABS at their own processing conditions for 3D printing (respectively 190 °C and 230 °C) [14-16]. Furthermore, glycerol-plasticized zein has efficient sintering abilities, also similar to standard printed materials [17, 18]. These fusion-bonding abilities, resulting from both surface tension (as a driving force) and viscosity (potentially limiting the sintering phenomenon) of the plasticized zein are of major interest to control the deposition of 3D printed structures consisting of juxtaposed and superimposed filaments [19].

Furthermore, zein can be plasticized directly by [Lidocainium][Ibuprofenate] ([Lid][Ibu]) [20]. This salt is an Active Pharmaceutical Ingredient - Ionic Liquid (API-IL), a new family of promising compounds for future drugs, because they can be easily dosed and processed, even thermo-mechanically, and constitute molecules showing better bioavailability and stability than solid forms [21].

In the case of zein, [Lid][Ibu] both favors processing and provides the final therapeutic properties after hot melt extrusion: From extruded filaments, a progressive release of this active ingredient was obtained in simulated physiological conditions, thanks to high affinity between zein and [Lid][Ibu].

Moreover, the zein-based matrix, which undergoes thermomechanical treatment for 3 minutes at 130 °C, demonstrates its structural integrity as evidenced by thermal gravimetric analysis (TGA), with the primary decomposition temperature observed above 250 °C. Additionally, during the same duration and temperature (3 minutes at 130 °C), the matrix retains both the anesthetic effect of Lidocaine and the analgesic effect of Ibuprofen [22].

In the present work, our objective is to combine glycerol and [Lid][Ibu] as co-plasticizers of zein in order to tune the 3D printing processability. We investigate in detail the rheological behavior, sintering properties, 3D printing abilities and porous structures of resulting plasticized zein-based materials. We first characterize the rheological properties of zein plasticized by various glycerol/API-IL ratios in steady-state flow under extrusion conditions and dynamic oscillatory testing. Then, the sintering abilities of plasticized zein are finely characterized with an original experimental set-up, based on the monitoring of the fusion-bonding kinetics between filaments by real-time X-ray microtomography using synchrotron radiation. Indeed, the impressive development of X-ray computed microtomography led to application in monitoring the sintering of powders with high resolution allowed by synchrotron radiation, in particular to qualify materials for additive manufacturing during powder particle laser sintering [23-25].

Nevertheless, it can also be applied to bigger objects such as filaments, benefiting from fast scans (hundreds of 2D radiographs acquired per second) and high resolution (typically below 10 µm voxel size) during a long period of several minutes for filaments viscous sintering with surface tension as sole driving force [26, 27]. Such time-resolved tomography, adapted for dynamic processes, could be of prime interest in testing materials as candidates for 3D printing by comparing their sintering abilities to standard synthetic polymers, or biopolymer-based printable materials [28]. These data are of special importance in order to guarantee an efficient adhesion to control the porosity and the release of active molecules included in the matrix for pharmaceutical applications.

Finally, based on these results, which lead to a more accurate definition of the processing window, zein-based tablets are 3D printed by hot melt extrusion and their porous structure is assessed with static X-ray tomography using laboratory equipment. This allows evaluating the potential of zein plasticized by glycerol and [Lid][Ibu] to be printed as drug delivery systems.

2. Materials and methods

2.1. Raw materials

All reagents used were of analytical grade. Zein-Z3625 and glycerol-G7893 were purchased from Sigma-Aldrich. The Active Pharmaceutical - Ionic Liquid (API-IL), [Lidocainium][Ibuprofenate], was synthesized as in Jouannin et al.'s study [29] and provided by the UTINAM Institute (UMR CNRS 6213, Université de Bourgogne Franche-Comté, Besançon, France).

2.2. Formulation

Physical mixtures of plasticized zein were prepared by adding plasticizers to powdery raw zein following Table 1. Powder was compressed into small tablets (Ø≈3 mm) to feed the single screw of the 3D printer during subsequent additive manufacturing trials.

Table 1. Formulations of zein-based materials, based on 100 g raw zein (5% water content) from supplier with added glycerol and/or API-IL [Lid][Ibu].

Formulation ID	Glycerol [g]	[Lid][Ibu] [g]
Z20GLY	20	0
Z15GLY5LI	15	5
Z10GLY10LI	10	10
Z5GLY15LI	5	15
Z20LI	0	20

2.3. Melt processing and rheological measurements

Rheological assessment was conducted under two distinct conditions: first one was under extrusion conditions, using either constant rotation speed of the screws or by varying the rotation speed. The second set of measurements was made under dynamic conditions using a cell with two parallel plates in oscillatory rotational movements.

2.3.1. Steady-state flow measurements in extrusion conditions

Steady-state flow measurements were carried out on melted materials using a micro-compounder (Haake Minilab, Thermo Scientific GmbH, Karlsruhe, Germany) to reproduce extrusion process conditions. The instrument can be used to circulate melt samples through a conical twin-screw system (L_{screw} = 12 cm) followed by a backflow channel (64 × 10 × 1.5 mm^3)

equipped with two pressure sensors, before their recirculation in a loop, or extrusion through the exit die.

Approximately 7 to 8 g of material were introduced in the system at 130 °C with a screw rotation speed of N = 50 rpm for steady shear rate measurements. Engine torque (T) was recorded, as well as pressure drop in the channel (ΔP) to calculate the apparent viscosity:

$$\eta_a = \frac{\tau}{\dot{\gamma}_a} \quad (1)$$

With τ (Eq. 2) the shear stress and $\dot{\gamma}_a$ (Eq. 3) the apparent shear rate,

$$\tau = \frac{h.\Delta P}{2.\Delta L} \quad (2)$$

$$\dot{\gamma}_a = \frac{6}{w.h^2} \cdot Q \quad (3)$$

where h = 1.5 mm and w = 10 mm are, respectively, the height and width of the channel, ΔL = 64 mm and ΔP, the length and the pressure drop between the sensors. Q is assumed as proportional to the screw rate according to

$$Q = C \cdot N\,, \quad (4)$$

with C = 6×10^{-10} m^3.s^{-1}.rpm^{-1}, a calibration constant obtained for a commercial polystyrene (LACQRENE® 6631) of known rheological behavior in co-rotative screws extrusion and N in rpm [30].

Measurements involving different screw rotation speeds were also conducted during the recirculation process within the micro-compounder, by decreasing the rotation speed in 10-second intervals from 200 rpm via the discrete values 150, 100, and 50 rpm down to 10 rpm during a cycle sweep. This cycle was repeated several times. For a backflow channel of such a rectangular geometry, values of viscosity (η) were calculated using corrected shear rate values in order to consider the shear-thinning properties of the materials and the dimensions of the channel [30, 31]. The slope of the curve $\log(\tau) vs \log(\dot{\gamma}_a)$ provides the pseudo plasticity index n that allows the Rabinowitsch correction

$$\dot{\gamma}_w = \dot{\gamma}_a \times \frac{2}{3}\left(1.047 + \frac{0.452}{n}\right) \quad (5)$$

2.3.2. Shear oscillation rheometry

Oscillatory measurements were performed using a rheometer with a plate-plate geometry pre-heated at 130 °C. Samples were placed between two parallel plates of $ø_{plate}$ = 20 mm diameter oscillating in order to apply a strain of γ_0 = 0.7% in the linear viscoelastic domain [16]. Approximately 0.5 g of extruded filaments obtained by direct extrusion using the micro-compounder (see the following paragraph, §2.3.1), were placed onto the basement plate to be melted for these oscillatory experiments. First series of measurements were done at constant frequency ω = 1.7 Hz (10 rad/s), shear viscosity η and elastic and viscous moduli G′ and G″ were recorded by the software device (Eq. 6, 7 and 8).

$$\eta^* = K \cdot \omega^{n-1} \quad (6)$$

$$G' = L \cdot \omega^{m} \quad (7)$$

$$G'' = P \cdot \omega^{r} \quad (8)$$

The second series of measurements consisted in frequency sweep with oscillation decreasing from ω ≈ 630 rad/s to 0.630 rad/s. This cycle was repeated over time for about 40 min.

2.4. Filaments sintering characterization

In order to fully investigate the thermoplasticization of zein, considering the presence of glycerol and/or other potential plasticizers, it is necessary to thoroughly characterize the sintering capabilities between the extruded filaments. To achieve this objective, it is crucial to go beyond the acquisition and analysis of 2D images to characterize the material while mitigating inherent limitations, primarily the drop-shadow effect caused by backlighting and the challenge of accurately locating the focal plane due to the length of filaments and their continuous movement during hot melt isothermal sintering in the instrumented oven.

166

167 *2.4.1. Experimental set up for synchrotron dynamic X-ray tomography*

168 The high intensity of the synchrotron X-ray beam is required to record data with sufficient
169 signal-to-noise ratio in a short time, here of the order of a few seconds per volume scan. The
170 availability of inline phase contrast is an additional plus over laboratory X-ray tomography. The
171 synchrotron X-ray tomography measurements were performed using the microtomography
172 station [32] at the ANATOMIX beamline [33] of Synchrotron SOLEIL. A furnace dedicated to
173 synchrotron microtomography at high temperatures (105 x 100 x 80 mm^3; heating power 40 W;
174 T in the range [100 °C; 140 °C] ±0.1 °C), was designed for this purpose by the BIA-INRAE
175 group in close exchange with the ANATOMIX beamline team (Fig. 1). The heated volume
176 inside the furnace is essentially a horizontal cylindrical cavity (⌀20 mm) lined with aluminum
177 and insulated with Teflon -polytetrafluoroethylene (PTFE), through which the synchrotron X-
178 ray beam can pass, with one Kapton window at each end to limit the thermal convection while
179 ensuring X-ray transmission near 100%. A vertical hole (⌀10.5 mm) in the bottom of the
180 chamber, also with aluminum lining, enables insertion of the sample from below. The furnace
181 was fixed on a vertical motorized translation, suspended above the tomography rotation stage.
182 Two extruded filaments based on zein ($\varnothing_{filament}$ = 2 mm, $L_{filament}$ = 5 mm) were placed side-by-
183 side on the flat top of the sample holder, a tailor-made cylindrical sample support (⌀10 mm)
184 made of PEEK and topped with an aluminum plate (thickness 1 mm). To carry out sintering
185 trials under isothermal conditions, the furnace was first heated up for 10 minutes at the desired
186 set temperature, while kept in a position 20 cm above the samples and the X-ray beam. Then it
187 was lowered in about 10 s over the samples and into the X-ray beam using the motorized
188 translation, enabling tomography scanning of the two filaments during their sintering thanks to
189 the high temperature of the pre-heated furnace.

190

a-

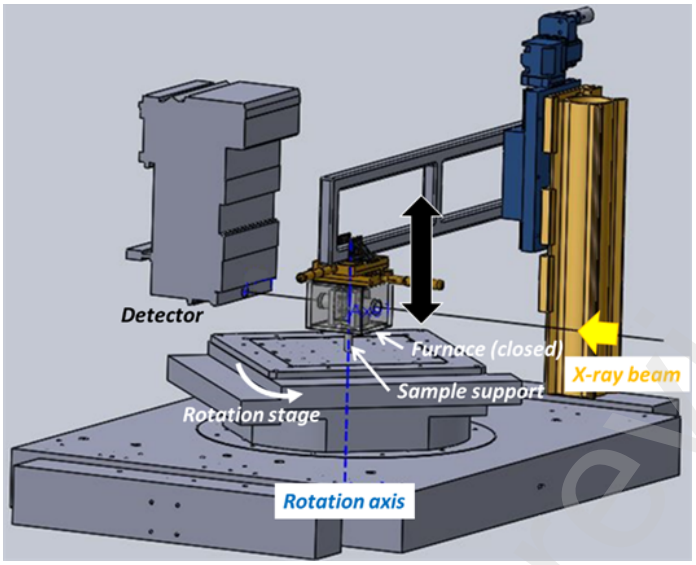

b-

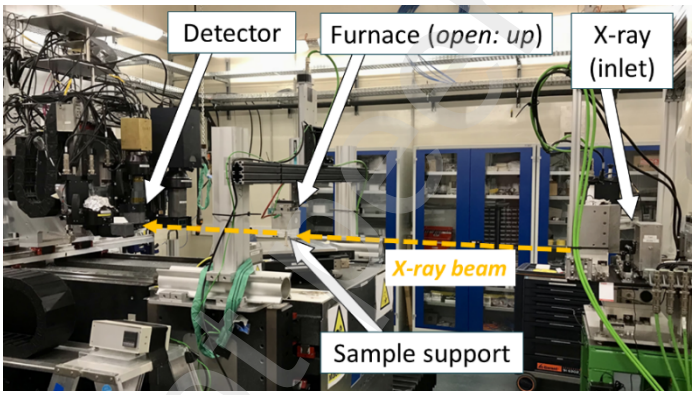

c-

d-

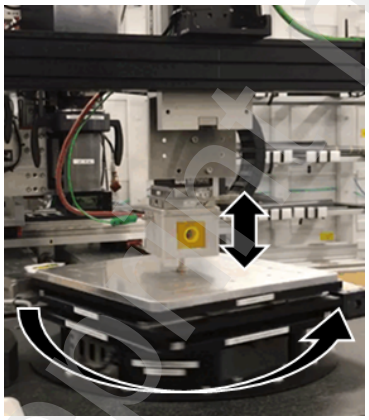

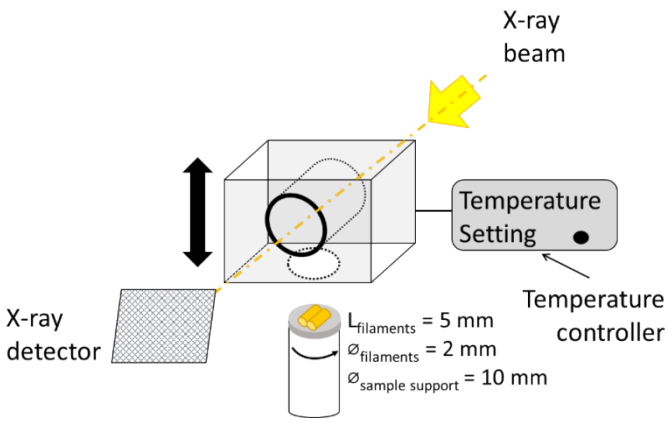

Fig. 1. Experimental set up for dynamic X-ray tomography at the ANATOMIX beamline to assess filaments sintering kinetics: (a) 3D drawing and (b) photo. (c) Front view of the furnace with Kapton window and (d) scheme of the devices and samples (*i.e.,* two juxtaposed filaments) placed on the holder.

Each tomography volume scan was performed by acquiring 1000 projection radiographs over an angular range of 180° while the sample stage (model RT500, LAB Motion Systems, Bekkevoort, Belgium) was rotated at a speed of $150°{\cdot}s^{-1}$. The overall acquisition time for the projections of each scan was thus 1.2 s, where the camera acquisition time for each projection was set to 1 ms. Scans were acquired every 6 s (*i.e.*10 $scans{\cdot}min^{-1}$) during 2.5 min.

The detector was an indirect lens-coupled system consisting of a single-crystal lutetium aluminum garnet scintillator ($Lu_3Al_5O_{12}$, thickness 300 µm, supplier: Crytur, Turnov, Czech Republic), a pair of Hasselblad photo objectives with focal lengths of, respectively, 100 mm and 210 mm mounted in tandem geometry [34], resulting in an optical magnification of 2.1, and a scientific-grade fast CMOS detector (model pco.dimax HS4; supplier: PCO, Kelheim, Germany; 2000 × 2000 pixels, physical pixel size 11 µm). The effective pixel size was 5.2 µm.

The beamline was operated with an electron current of 450 mA in the SOLEIL storage ring, using a filtered polychromatic ("white") X-ray beam from the U18 cryogenic in-vacuum undulator of the beamline set to a magnetic gap of 7.5 mm and X-ray attenuation filters of gold with a total Au thickness of 20 µm, resulting in a central X-ray photon energy around 25 keV. At the camera exposure time of 1 ms, this gave a signal of 26,000 ADU (analog-digital units) in the flat beam from the 16-bit analog-digital converter (ADC) of the pco.dimax.

The camera was operated with a hardware region of interest (ROI) set to 1600 × 560 pixels, *i.e.* a field of view of 8.3 mm width and 2.9 mm height. The distance between the sample and the detector was set to 760 mm, to allow for X-ray phase contrast to form, in order to be sensitive to potential defects in the filaments, such as pores. Tomographic reconstruction was performed using the standard data processing pipeline at ANATOMIX, in which reconstruction parameters are set with an iPython script [35] and the reconstruction itself was performed by the computer program PyHST2 [36] using the filtered back-projection method.

2.4.2. Image analysis to characterize sintering kinetics

Image analysis and adjustments are semi-automated and carried out with Matlab® software (The MathWorksInc, Natick, MA, US). For image analysis, the 3D reconstructed volumes stored in 32-bit floating-point format obtained from X-ray tomography were first converted into 8-bit files to reduce the computational time. For each 3D image, an adapted median filter was applied to remove noise, and a grey level threshold was determined to segment the sample from the background. This threshold was set to the median value of the first pixels analyzed on the image. Subsequent image processing consisted of morphological filters to reduce the artefacts at the edges of the filaments in order to obtain binary images of a ROI corresponding to the filaments, faithful to the experimental phenomenon. From these binary images, virtual sections with a total thickness of 57 µm (stack of 11 slices of the image x 5.2 µm thick each) were selected in the center part of the two juxtaposed filaments to characterize the sintering phenomenon in detail (Fig. 2). Those 11 segmented slices were combined with a logical "OR" operation into a single 2D image. The length of the fusion bonding neck between the two filaments and the corresponding bonding angle was calculated following Hopper's model [17, 37].

a- b- c-

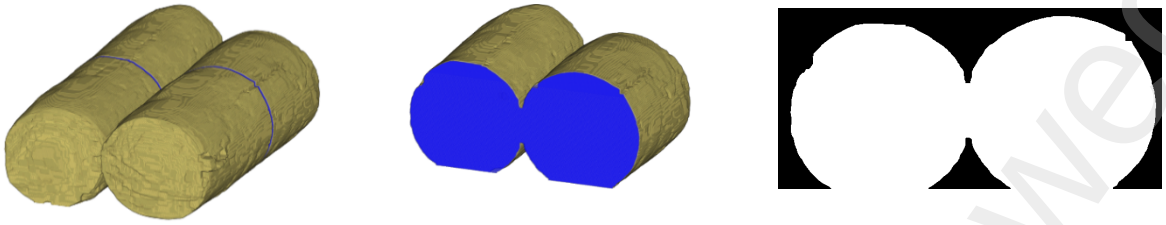

Fig. 2. Illustration of the characterization of sintering between two extruded zein-based filaments (formulation Z20GLY, after 100 s at 130 °C) from dynamic X-ray tomography. Three steps: (a) 3D rendering of the whole volume of the juxtaposed filaments; (b) 3D rendering cut in half at the location to monitor fusion-bonding between filaments; (c) 2D segmented image of the section shown in blue in (a) and (b) with the zein-based material in white pixels and surrounding air in black.

234

235 Hopper's model was then used to assess the evolution of the geometry of the sintered filaments
236 with time at high temperature in the furnace: the length of the fusion bonding neck, L_{min}, the
237 average maximum diameters of the right (R) and left (L) filament seen as side view, L_{max}, and
238 the bonding angle θ (Fig. 3).

239 $$L_{max} = \frac{L_{maxR} + L_{maxL}}{2} \quad (9)$$

240 $$\theta = sin^{-1}\left(\frac{L_{min}}{L_{max}}\right) \quad (10)$$

241

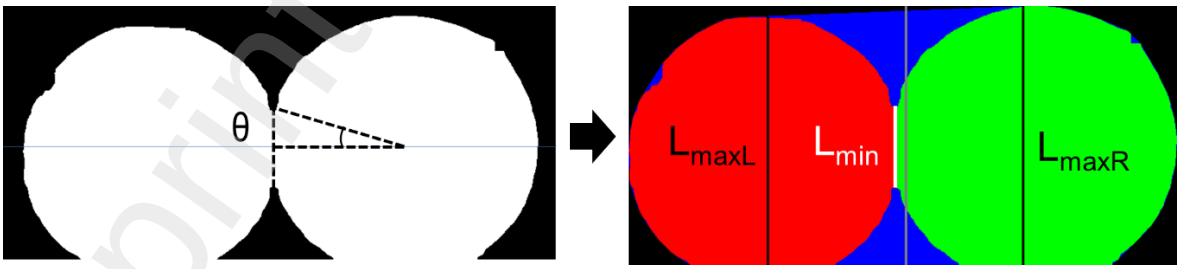

Fig. 3. Left: Binary segmented image of a filament cross-section during sintering (stack of 11 tomographic slices in the middle part of the filaments during their sintering; Z20GLY sample at 130 °C after ~100 s in the furnace). Right: illustration of the quantities retrieved by image analysis.

242

243 *2.5. Additive manufacturing*

244 Model cylindrical tablets were 3D printed with formulations based on zein in collaboration with
245 West Waste Print (Nantes, France), Octoplus-3D (Barjouville, France) and 3D printer
246 manufacturer Tumaker® (Irun, Spain). A 3D printer by hot melt deposition with a single screw
247 ($Ø_{screw}$ = 8 mm) was equipped with a 0.8-mm-diameter nozzle. Layers of 0.4 mm were
248 produced with an extruding rate of 25 mm/s (setting at 750 step.mm^{-1} for the step-by-step
249 engine). The extrusion temperature (barrel of the single-screw extruder) was set at 115 °C and
250 the nozzle temperature at 140 °C (to obtain a temperature of the flowing material measured at
251 about 130 °C, because of heat loss, the printer environment being open). The plate was
252 regulated at 100 °C, to obtain temperature on the surface above 80 °C (the temperature for
253 material flowing [16]). Six successive layers were superimposed for 3D printed tablets, to reach
254 a total thickness of about 2.4 mm. Two types were processed based on zein-based materials:
255 $Ø_{tablets}$ = 35 mm, for three complex porous structures presenting the same density at 0.5 but
256 different printed porous patterns and $Ø_{tablets}$ = 20 mm for dense -*100% infill*- model, needing
257 less place to obtain a simple rectilinear non-patterned porous structure).

258

259 *2.6. Static X-ray tomography scans at laboratory scale*

260 Static X-ray tomography images were obtained using a Skyscan 1174 apparatus (Bruker France
261 SAS, Champs-sur-Marne, France) located at Oniris (Nantes, France). Samples were placed in
262 a foam support and scanned in rotation steps of 0.6°, for a total exposure time of about 20 min.
263 The reconstructed slices obtained were TIFF files of 16-bit depth and a pixel size of 29.7 µm.

264

265 **3. Results and discussion**

266 *3.1. Steady-state flow rheology under extrusion conditions*

Measurements carried out with the twin-screw micro-compounder allow screening formulations of zein plasticized by various amounts of glycerol and/or [Lid][Ibu], by comparing their rheological behavior as a function of residence time (Fig. 4).

Apparent viscosity values measured after 1 min of recirculation are given in Table 2. Plasticization with the same amount of pure glycerol (Z20GLY) leads to a much lower melt viscosity compared to pure [Lid][Ibu] (Z20LI). This may be attributed to a different plasticization mechanism of the amphiphilic zein macromolecules, which have a prismatic structure combining hydrophilic top and bottom surfaces and hydrophobic lateral surfaces [38]. Glycerol being hydrophilic and [Lid][Ibu] hydrophobic, the two substances can only interact with the respective matching surfaces of zein prisms. Viscosity values thus suggest that the overall reduction of zein intermolecular interactions is higher for glycerol which reduces the hydrophilic interactions between zein prisms. When glycerol is partially substituted by 5% of [Lid][Ibu] (Z15GLY5LI), the initial viscosity slightly decreases suggesting a synergy between the two plasticization mechanisms. However, for higher [Lid][Ibu] content, the viscosity increases almost linearly.

Table 2. Apparent initial viscosity of zein-based materials after 1 min recirculating in twin-screw micro-compounder at 130 °C and duration of the processing window *i.e.* time to protein aggregation.

Formulation ID	Apparent initial viscosity at t=1 min [Pa.s]	Duration of the processing window [min]	Gelation time [min]
Z20GLY	770	6	12
Z15GLY5LI	750	9	26
Z10GLY10LI	970	10	92
Z5GLY15LI	1020	-	286
Z20LI	1330	-	

During the recirculation inside the micro-compounder at 130 °C, the viscosity increases with time for all formulations. However, the shape of viscosity vs time curves strongly differs. For pure [Lid][Ibu] (Z20LI), a sharp, almost linear increase is observed, reaching $5.4x10^3$ Pa.s after approximately 180 sec (Fig. 4). This suggests a fast aggregation of zein macromolecules by stacking of their hydrophilic top and bottom surfaces [38]. Such a rheological behavior is incompatible with a melt 3D printing process. Concurrently, for pure glycerol plasticization, the slope of the viscosity curve remains low for approximately 360 sec (6 min) before increasing to above $2x10^3$ Pa.s. This leaves a time window for 3D printing, before zein macromolecules aggregation by side-by-side association through hydrophobic residues, and/or sulfide bond formation (the cysteine residues being hydrophobic).

It is noteworthy that the partial substitution of glycerol by up to 50% of [Lid][Ibu] (Z10GLY10LI) increases the processing window before the change of slope, suggesting a synergy between the plasticizers in terms of delaying protein aggregation, both through their hydrophobic and hydrophilic residues. The formulation Z10GLY10LI thus combines a

relatively low initial viscosity, and a large processing window. It was therefore selected for further investigation for 3D printing of zein material based with pharmaceutical ingredient.

a-

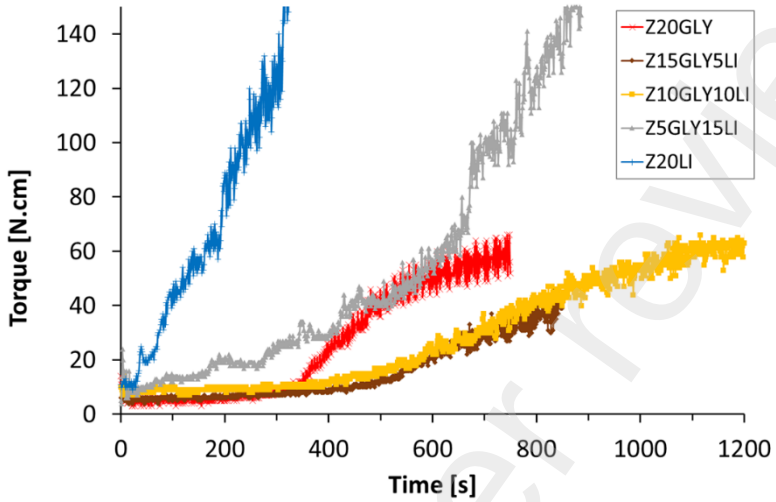

b-

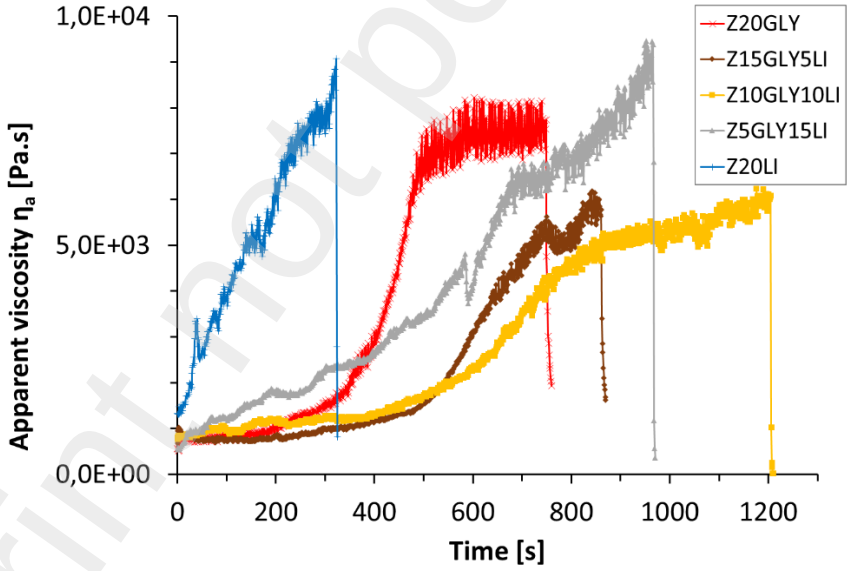

Fig. 4. (a) Engine torque and (b) apparent viscosity, η_a, of molten zein-based materials recirculating in the micro-compounder at 130 °C.

For Z20GLY and Z10GLY10LI, the flow curves obtained from measurements at various rotation rates are shown in Figure 5. Melt viscosity decreases with the increase of shear rate,

showing the shear thinning behavior of the materials, and increases with residence time at 130 °C as flow curves are shifting upward. This corresponds to protein aggregation, as mentioned above in paragraph §3.1.1. (Fig. 5). Cycle 1 (residence time ≈ 1 min) highlights the lower initial viscosity of formulation Z20GLY compared to Z10GLY10LI with an apparent viscosity between 260 and 1000 Pa·s, against 560-1700 Pa·s for Z10GLY10LI. Measurements of the following cycles show greater shear-thinning properties for Z20GLY, as viscosity gap between the highest and the lowest shear rate is around $5x10^3$ Pa·s against $2x10^3$ Pa·s for Z10GLY10LI. However, rheological properties of Z20GLY seem to reach a plateau from cycle 3 (≈ 8 min), as curves of the following cycles are superimposed, whereas curves of Z10GLY10LI continue to shift to higher viscosity values. This behavior demonstrates the protein aggregation as being delayed when formulation includes 10% of [Lid][Ibu] (Z10GLY10LI).

a-

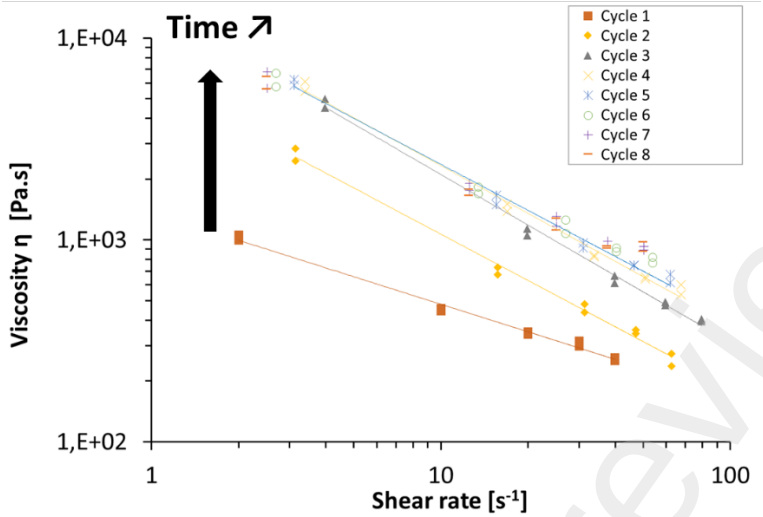

b-

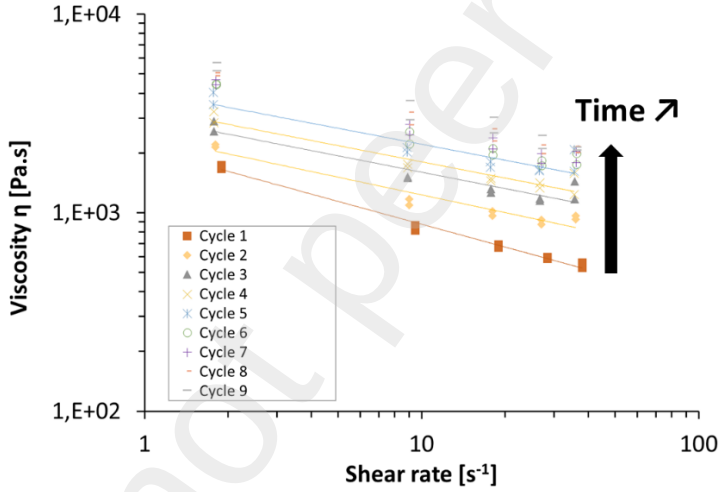

Fig. 5. Evolution of the viscosity, η, determined during recirculation in micro-compounder at 130 °C and presented as a function of the applied shear rate for zein-based materials: (a) Z20GLY, (b) Z10GLY10LI. Each cycle corresponds to 5 rotation rates of the screws repeated over time (approximately at cycle 1: 1 min, cycle 4: 10 min, cycle 8: 25 min).

319

320 *3.2. Dynamic shear rheology*

321 Formulation Z10GLY10LI was characterized in plate-plate geometry rheometer in order to
322 assess its viscoelastic and rheological properties over a frequency range of several decades,
323 allowing to complete the comparison to the reference formulation Z20GLY, including glycerol
324 alone as standard plasticizer. Extruded filaments were melted in a parallel-plate rheometer at

130 °C to measure viscoelastic moduli along oscillations. Heating started with an elastic modulus G′ inferior to viscous modulus G″, as can be seen in Figure 6, confirming the melted state of the material. After several minutes at high temperature, moduli eventually increased and the G′ and G″ values converged up to crossover in the case of Z20GLY indicating a gelation of the material at t = 6 min. In presence of [Lid][Ibu] (Z10GLY10LI), such a crossover of the modulus curves was not observed during experiments, which can be ascribed either to an insufficient residence time at 130 °C to reach gelation, or to an absence of gelation. Indeed, gelation of plasticized zein is known to involve the formation of sulfide bonds by reaction between cysteine residues [16], which are hydrophobic. The presence of the hydrophobic [Lid][Ibu] thus may prevent such crosslinking reactions (and so gelation) or at least delay them. Assuming a simple delay of gelation, the time of crossover between G′ and G″ can be evaluated by asymptotic extrapolation of the curves, leading to the gelation time values listed in Table 2.

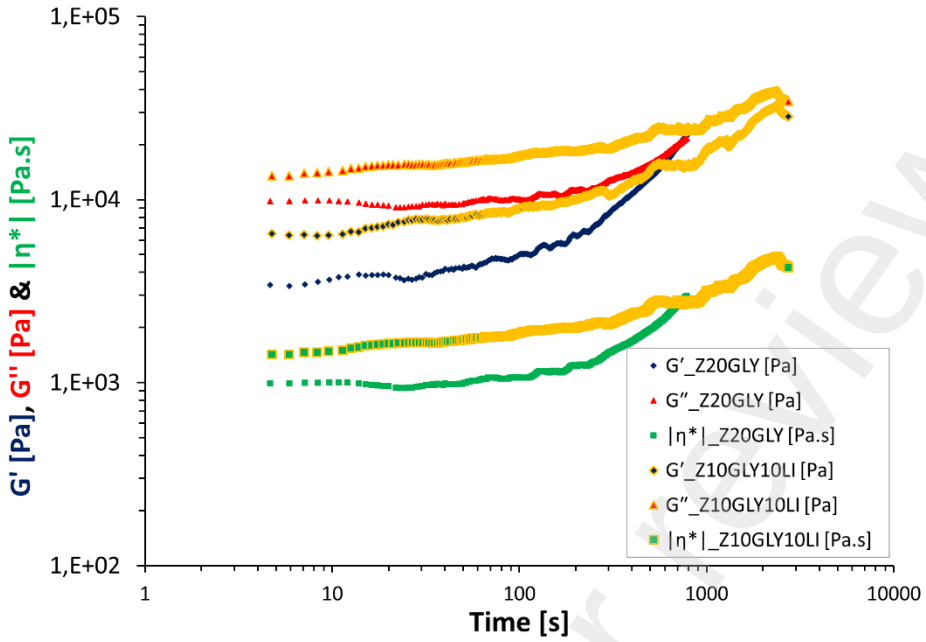

Fig. 6. Evolution of the viscoelastic behavior (*i.e.* conservative modulus G′ and dissipative one G″) and the modulus of the complex viscosity η*, obtained at 130 °C in an oscillation rheometer at constant frequency (1.7 Hz), for molten zein-based materials Z20GLY and Z10GLY10LI.

Measurements of viscoelastic modulus were also carried out in oscillatory frequency sweep with the same experiment. Figure 7 shows the first cycle of measurements at time ≈ 1 min. Viscosity decreases with the increase of the frequency showing the shear thinning properties of formulations. Z20GLY shows a lower viscosity. than Z10GLY10LI. This viscosity curve is shifting to higher values when cycles are repeated at high temperature and during these cycles, it is also interesting to note that the viscous modulus G″ is superior to G′ that tends to approach G″ when frequency oscillation increases and with viscosity increase (please see Appendix A1, Fig. S1).

The viscosity values obtained can be compared to the viscosity measured in cycle 1 with micro-compounder – recirculation – rotation speed sweep, and almost follow the application of the Cox-Merz empirical rule. For a minimum shear rate, at 1 rad/s and short heating (cycle 1), Z20GLY exhibits a lower viscosity (≈2 kPa·s) than Z10GLY10LI (≈3 kPa.s).

a-

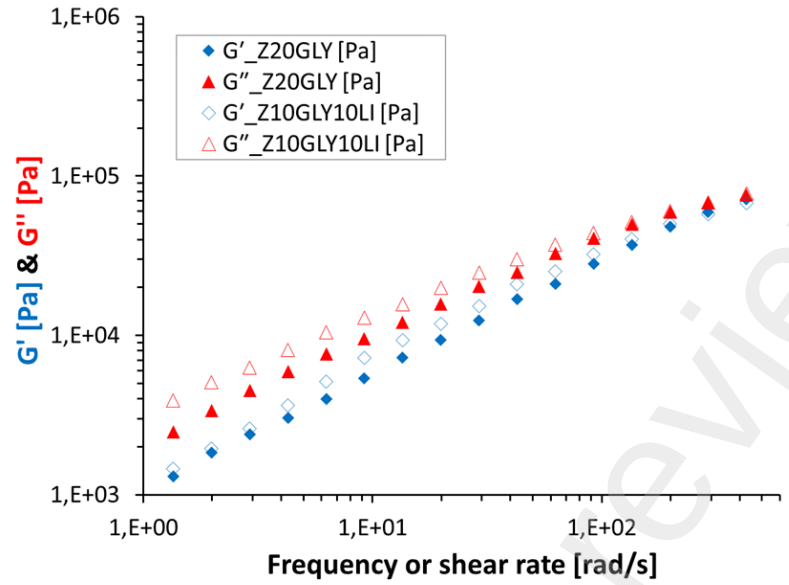

b-

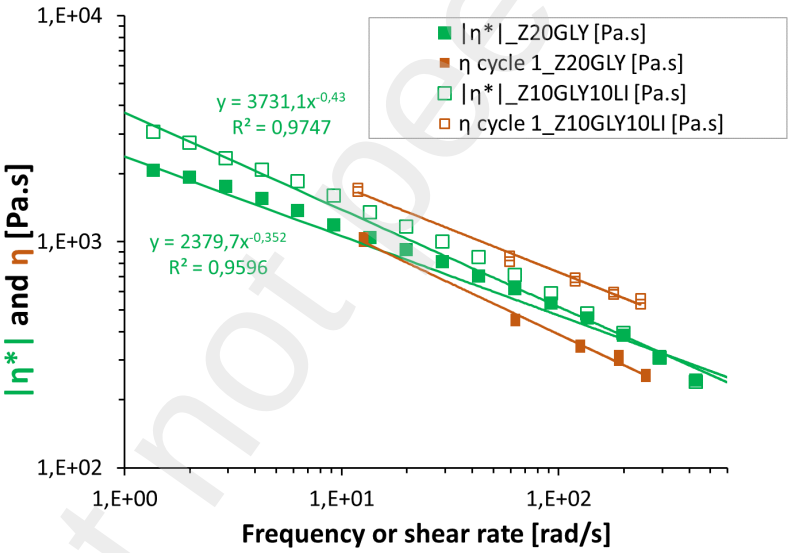

Fig. 7. Viscoelastic behavior assessed during the first frequency sweep at 130 °C for materials Z20GLY (filled squares) and Z10GLY10LI (hollow squares). (a) Values of the conservative modulus, G′, and the dissipative modulus, G″. (b) Modulus of the complex viscosity η* and superimposed values of the initial flow viscosity η (cycle 1) obtained under extrusion conditions with the micro-compounder set at 130 °C.

352

353 *3.3. Filament sintering abilities in relation to melt rheological behavior*

354 Figure 8 shows the evolution of the bonding angles obtained by image analysis of X-ray
355 tomography data for formulations Z20GLY and Z10GLY10LI at four temperatures ranging
356 from 100 °C to 140 °C.

357 The slope of the curves, initially close to zero, starts increasing around 50 s after the start of the
358 sintering process, except for the measurements at 100 °C, for which sintering remains very
359 slow, due to the fact that the molten state is only reached at temperatures significantly above
360 80 °C [16].

361

a-

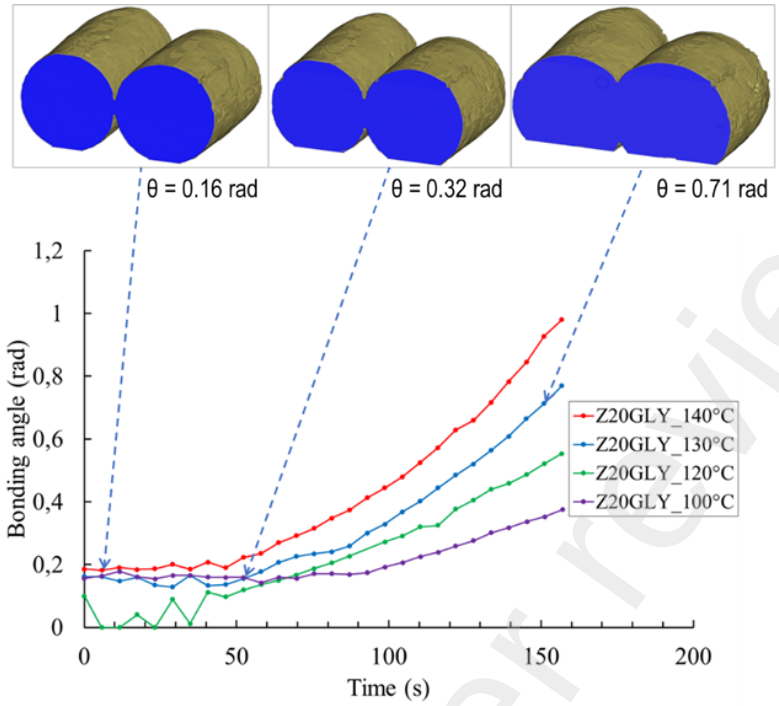

b-

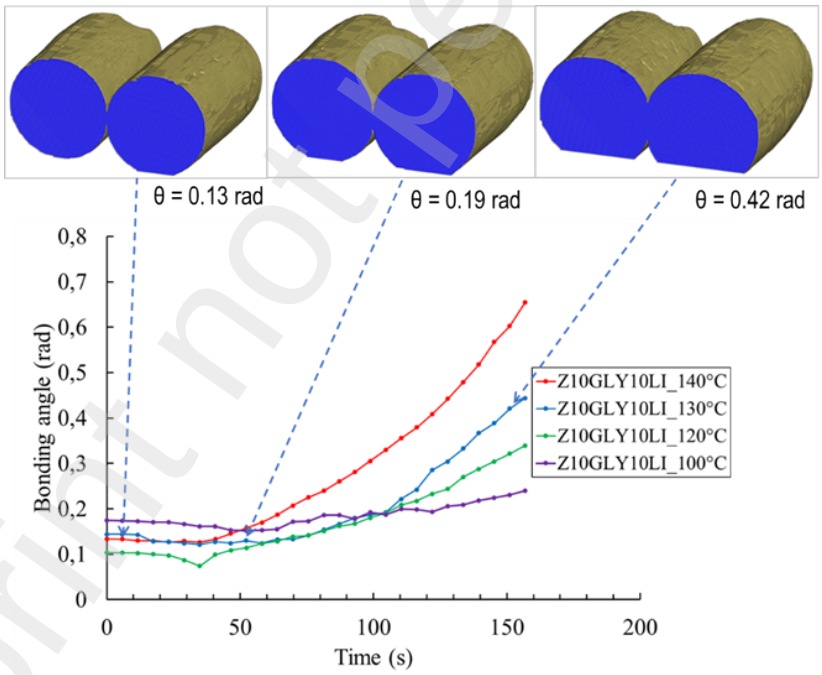

Fig. 8. Sintering kinetics monitored via the evolution of the bonding angles assessed by dynamic X-ray tomography for Z20GLY (a) and Z10GLY10LI (b).

362

Sintering rates V [rad.s^{-1}], defined as the slope of the linear part of the curves (in the range between 100 and 150 s) are given in Table 3: An increase with temperature is observed, as previously found for such plasticized biopolymer [17].

Lower rates are observed when [Lid][Ibu] is present, which is consistent with the higher melt viscosity compared to pure glycerol. It was also checked that no dilation force was involved in the fusion-bonding phenomenon, indeed, measurements carried out on one filament in the furnace showed no volume increase (please see Appendix A2, Fig. S2).

At temperatures above 100 °C, the ratio between the sintering rates observed for the two formulations is almost constant ($V_{Z10GLY10LI}$ / V_{Z20GLY} ≈ 60±5%). This ratio is close to that of melt viscosities at 130 °C measured after 150 s at 130 °C (typical sintering time) with micro-compounder during rotation rate sweeps measurements (η_{Z20GLY} / $\eta_{Z10GLY10LI}$ ≈ 61% at 10 rad·s^{-1}, Fig. 7-b) and in dynamic rheometry ($|\eta^*|_{Z20GLY}$ / $|\eta^*|_{Z10GLY10LI}$ ≈ 68 % at 1 rad·s^{-1} and $|\eta^*|_{Z20GLY}$ / $|\eta^*|_{Z10GLY10LI}$ ≈ 61% at 10 rad.s^{-1}, Fig. 7-b and Fig. 6, respectively). This suggests that the surface tension, the other parameter affecting sintering rate theoretically, is probably not significantly modified by the presence of [Lid] [Ibu].

Table 3. Sintering rate of Z20GLY and Z10GLY10LI and their ratio at different temperatures *(*beginning of the sintering phenomenon, slightly starting at 100 °C)*.

	V [rad.s^{-1}]		
Temperature [°C]	Z20GLY	Z10GLY10LI	*Ratio:* $V_{Z10GLY10LI}$ / V_{Z20GLY}
140	0.0093	0.0060	*65%*
130	0.0075	0.0047	*63%*
120	0.0050	0.0028	*56%*
*100**	*0.0032*	*0.0008*	*25%*

383

384 *3.4. 3D printed tablets based on zein and sintering abilities of the deposited melts*

385 Three virtual structures were generated by multi-physics modelling with identical 50% infill
386 density, leading to different simulated release kinetics (ST1, ST2 and ST3 from [12], Fig. 9).

387

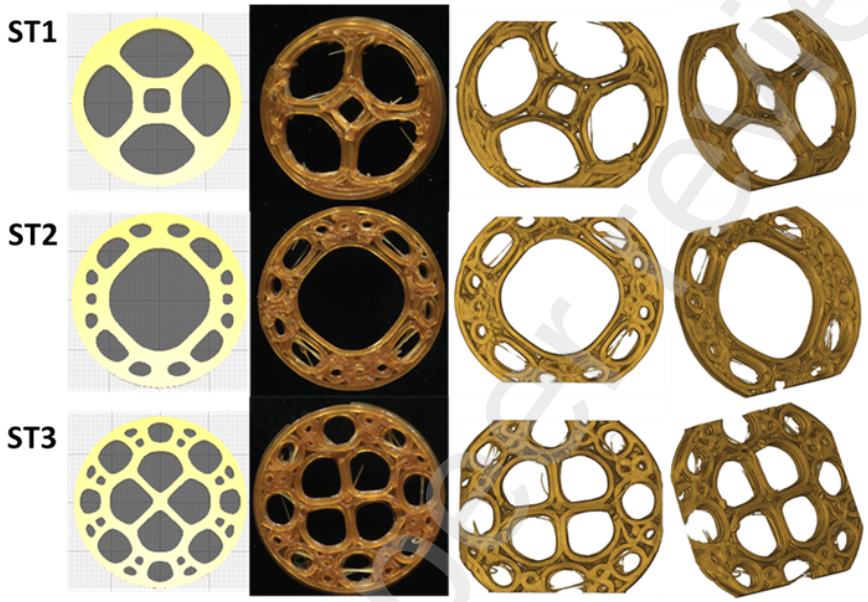

Fig. 9. 3D digital models of tablets with different geometries for the same density set at 0.5 (left); images of Z20GLY-printed tablets (left center) and 3D renderings of volumes obtained by static X-ray tomography with a laboratory instrument (right center and right).

388

389 These tablets were successfully printed with the Z20GLY formulation under conditions
390 described in paragraph §2.5, with a final porosity of the 3D printed tablets confirmed by X-ray
391 tomography to be 0.5 on average, with minimum and maximum values of, respectively, 0.47
392 and 0.55, confirming the suitability of zein plasticized with glycerol for 3D printing (Fig. 10).
393 However, experiments using the Z10GLY10LI formulation were inconclusive and revealed
394 poor adhesion of successive layers to one another. (Fig. 10-c). It is nonetheless noticeable that
395 the adhesion to platform support is very efficient for all tested compositions in 3D printing
396 trials.

397

a-

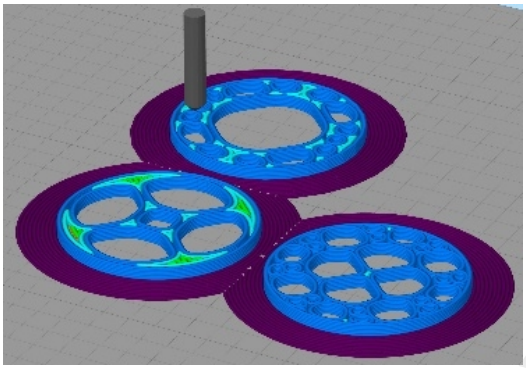

b-

c-

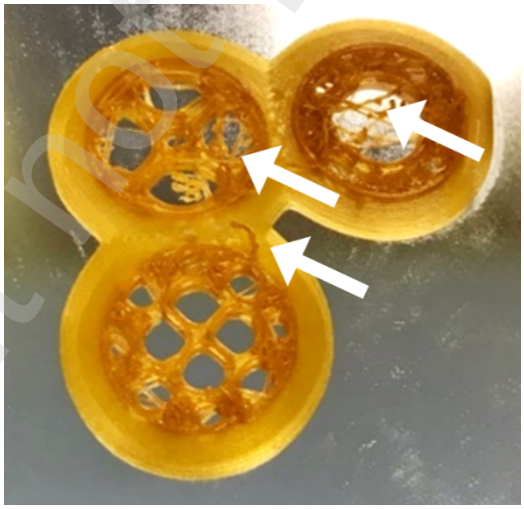

Fig. 10. Preview of melt deposition paths for 3D printing with different geometries (a), after 3D printing of Z20GLY (b) and Z10GLY10LI (c). Arrows indicate adhesion defects.

398

399 To enhance the printing of co-plasticized formulation Z10GLY10LI, we tried to optimize the

400 process conditions by working on full filled tablets (100% density in printing parameters, with

rectilinear filling). Z20GLY was correctly printed (Fig. 11-a) and, to obtain satisfying tablets with Z10GLY10LI (Fig. 11-b), the nozzle temperature set in the software was increased by 5 °C, as well as the extruded material flow rate that was increased by 15% (860 steps·mm^{-1} for the step-by-step engine). These conditions allowed us to overcome the higher viscosity of Z10GLY10LI, which leads to degraded sintering abilities as shown in the previous paragraph (§3.3).

The porous structure of the final printed tablets was tested by static X-ray tomography at the laboratory scale and, as expected, these tablets showed a very low porosity ranging from 0.5 to 1%. Furthermore, to help in adhesion, the flow rate was set significantly higher for Z10GLY10LI. Therefore, the tablet obtained with this formulation has the smallest porosity (0.5% in volume of the total printed part, Fig. 11). However, it is noteworthy that in the reconstructed volumes obtained through tomography, the pores within the Z20GLY tablet exhibit a higher level of connectivity compared to the Z10GLY10LI tablet. This observation confirms the greater density of the latter formulation. Moreover, porosity distribution is more in the small pores for Z10GLY10LI, with 80% pores smaller than 90 µm, whereas it is 55% in the case of Z20GLY (Fig. 11-c).

a-

b-

c-

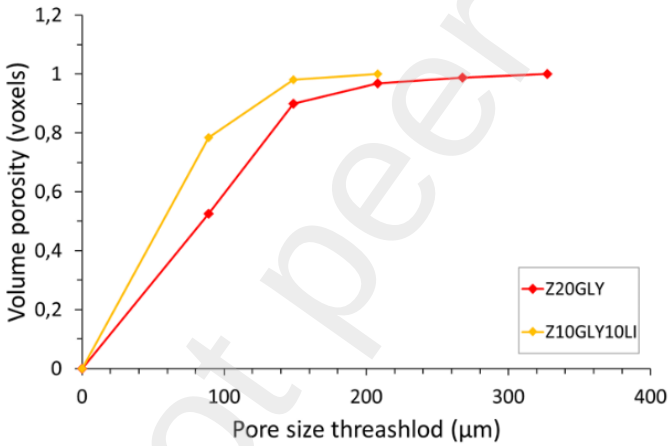

Fig. 11. 3D printed full-filled tablets ($Ø_{tablets}$ = 20 mm; 100% filling in melt deposition settings as rectilinear pattern) based on formulation: (a) Z20GLY and (b) Z10GLY10LI. Photos on the left hand and in-line visualization to the right of the reconstructed 3D volumes (static X-ray tomography at laboratory scale): dense material (superposition of 6 layers visible on the edge of the slightly rotated volume) and internal porosity linked to the "defect" during melt deposition. (c) Cumulative size distribution of pores (total porosity of the final printed tablets measured at 1% for Z20GLY and 0.5% for Z10GLY10LI).

4. Conclusions

This work has demonstrated that glycerol can be combined with a hydrophobic ionic liquid in order to tune the melt rheology of plasticized zein as a feedstock material for additive manufacturing by hot melt deposition. This technique enables the production of edible materials

including an Active Pharmaceutical Ingredient in the form of an Ionic Liquid (API-IL) for the formulation of 3D printed tablets intended for therapeutic purposes.

Flow rheology results obtained on a micro-compounder simulating extrusion at 130 °C showed that while zein-based melts show a shear thinning behavior, apparent viscosity of plasticized zein increases with API-IL/glycerol ratio and with residence time. However, adding the [Lidocainum][Ibuprofenate] API-IL to glycerol delays protein aggregation at 130 °C and broadens the time window for processing, from 6 minutes when 20w% of glycerol was used as sole plasticizer to 10 minutes in the case of co-plasticization by 10w% of glycerol and 10w% of API-IL. This was attributed to [Lid][Ibu] being hydrophobic while glycerol is hydrophilic. The two substances therefore interact with the amphiphilic zein macromolecules by different plasticization mechanisms. Nonetheless, this synergy between the plasticizers was not observed for higher amounts of [Lid][Ibu]. Indeed, the protein aggregation cannot be completely avoided and the evolution of zein-based melts' viscoelastic behavior studied with oscillatory testing suggested that a crossover of G′ and G″, *i.e.* a gelation phenomenon, takes places after longer durations with increasing amount of API-IL.

The partial substitution of glycerol by API-IL also affects the melt sintering kinetics, which were assessed via a purpose-built dedicated motorized furnace for real-time synchrotron X-ray microtomography 3D imaging. It was used to monitor the fusion-bonding kinetics of extruded filaments in high resolution, during isothermal trials. Viscous sintering kinetics were faster when the temperature was increased in the range from 100 °C to 140 °C, but slowed down when increasing the API-IL content, presumably due to the induced viscosity increase.

Subsequent 3D printing tests at 130 °C showed that such slowed sintering kinetics limits the printing accuracy of the glycerol/API-IL co-plasticized formulation, despite well bonded juxtaposed and superimposed layers, while the formulation including glycerol as sole

plasticizer allows printing tablets with complex porous structures characterized in detail by static X-ray tomography.

These results open the way for future work on 3D geometries based on zein and Active Pharmaceutical Ingredients as Ionic Liquid, targeting applications in the biomedical or the pharmaceutical field by taking advantage of both their plasticizing and therapeutic properties to set edible and functional printed systems.

Acknowledgements

The authors would like to thank Dr. Y.-M. Corre (ComposiTIC, UBS, Ploemeur, France), M. T. Lecoq (West Waste Print, Nantes, France) and Octoplus 3D (Barjouville, France) for 3D printing trials. The synchrotron microtomography experiment was carried out via SOLEIL beamtime proposal no. 20220020. ANATOMIX is an Equipment of Excellence (EQUIPEX) funded by the *Investments for the Future* program of the French National Research Agency (ANR), project *NanoimagesX,* grant no. ANR-11-EQPX-0031. The authors would particularly like to thank G. Daniel of Synchrotron SOLEIL for technical support before and during the synchrotron tomography experiment. The authors would also like to thank Dr. L. Viau (UTINAM Institute, UMR CNRS 6213, Université de Bourgogne Franche-Comté, Besançon, France) for the synthesis of [Lidocainium][Ibuprofenate], the Active Pharmaceutical Ingredient-Ionic Liquid used in the present study and Dr. S. Florin-Muschert (Inserm U 1008/ Laboratoire de Pharmacotechnie industrielle/ UFR3S - Pharmacie, Université de Lille, France) for materials tablets preparation. This work was supported by the Region Pays de la Loire.

References

[1] G. Chen, Y. Xu, P.C.L. Kwok, L. Kang, Pharmaceutical Applications of 3D Printing, Addit Manuf. 34 (2020) 101209. https://doi.org/10.1016/j.addma.2020.101209.

[2] L. Rodríguez-Pombo, A. Awad, A.W. Basit, C. Alvarez-Lorenzo, A. Goyanes, Innovations in Chewable Formulations: The Novelty and Applications of 3D Printing in Drug Product Design, Pharmaceutics. 14 (2022). https://doi.org/10.3390/pharmaceutics14081732.

[3] M.-M. Germaini, S. Belhabib, S. Guessasma, R. Deterre, P. Corre, P. Weiss, Additive manufacturing of biomaterials for bone tissue engineering – A critical review of the state of the art and new concepts, Prog Mater Sci. 130 (2022) 100963. https://doi.org/10.1016/j.pmatsci.2022.100963.

[4] A. Goyanes, A.B.M. Buanz, A.W. Basit, S. Gaisford, Fused-filament 3D printing (3DP) for fabrication of tablets, Int J Pharm. 476 (2014) 88–92. https://doi.org/10.1016/j.ijpharm.2014.09.044.

[5] A. Goyanes, N. Allahham, S.J. Trenfield, E. Stoyanov, S. Gaisford, A.W. Basit, Direct powder extrusion 3D printing: Fabrication of drug products using a novel single-step process, Int J Pharm. 567 (2019). https://doi.org/10.1016/j.ijpharm.2019.118471.

[6] K. Ilyés, N.K. Kovács, A. Balogh, E. Borbás, B. Farkas, T. Casian, G. Marosi, I. Tomuță, Z.K. Nagy, The applicability of pharmaceutical polymeric blends for the fused deposition modelling (FDM) 3D technique: Material considerations–printability–process modulation, with

consecutive effects on in vitro release, stability and degradation, European Journal of Pharmaceutical Sciences. 129 (2019) 110–123. https://doi.org/10.1016/j.ejps.2018.12.019.

[7] G.M. Khalid, N. Billa, Solid Dispersion Formulations by FDM 3D Printing—A Review, Pharmaceutics. 14 (2022). https://doi.org/10.3390/pharmaceutics14040690.

[8] S. Abdella, S.H. Youssef, F. Afinjuomo, Y. Song, P. Fouladian, R. Upton, S. Garg, 3D printing of thermo-sensitive drugs, Pharmaceutics. 13 (2021). https://doi.org/10.3390/pharmaceutics13091524.

[9] J.R. Cerda, T. Arifi, S. Ayyoubi, P. Knief, M. Paloma Ballesteros, W. Keeble, E. Barbu, A. Marie Healy, A. Lalatsa, D.R. Serrano, Personalised 3d printed medicines: Optimising material properties for successful passive diffusion loading of filaments for fused deposition modelling of solid dosage forms, Pharmaceutics. 12 (2020). https://doi.org/10.3390/pharmaceutics12040345.

[10] B.M. Boyle, P.T. Xiong, T.E. Mensch, T.J. Werder, G.M. Miyake, 3D printing using powder melt extrusion, Addit Manuf. 29 (2019). https://doi.org/10.1016/j.addma.2019.100811.

[11] A. Cano-Vicent, M.M. Tambuwala, Sk.S. Hassan, D. Barh, A.A.A. Aljabali, M. Birkett, A. Arjunan, Á. Serrano-Aroca, Fused deposition modelling: Current status, methodology, applications and future prospects, Addit Manuf. 47 (2021) 102378. https://doi.org/10.1016/j.addma.2021.102378.

[12] L. Chaunier, S. Guessasma, S. Belhabib, G. Della Valle, D. Lourdin, E. Leroy, Material extrusion of plant biopolymers: Opportunities & challenges for 3D printing, Addit Manuf. 21 (2018) 220–233. https://doi.org/10.1016/j.addma.2018.03.016.

[13] L. Bisharat, H.S. Alkhatib, A. Abdelhafez, A. Barqawi, A. Aljaberi, S. Qi, A. Berardi, Hot melt extruded zein for controlled delivery of diclofenac sodium: Effect of drug loading and medium composition, Int J Pharm. 585 (2020) 119503. https://doi.org/10.1016/j.ijpharm.2020.119503.

[14] G.P. Kar, S. Biswas, S. Bose, Tailoring the interface of an immiscible polymer blend by a mutually miscible homopolymer grafted onto graphene oxide: Outstanding mechanical properties, Physical Chemistry Chemical Physics. 17 (2015) 1811–1821. https://doi.org/10.1039/c4cp04481a.

[15] S.W. Hwang, D.H. Park, D.H. Kang, S.B. Lee, J.K. Shim, Reactive compatibilization of poly(l-lactic acid)/poly(propylene carbonate) blends: Thermal, thermomechanical, and morphological properties, J Appl Polym Sci. 133 (2016). https://doi.org/10.1002/app.43388.

[16] L. Chaunier, G. Della Valle, M. Dalgalarrondo, D. Lourdin, D. Marion, E. Leroy, Rheology and structural changes of plasticized zeins in the molten state, Rheol Acta. 56 (2017) 941–953. https://doi.org/10.1007/s00397-017-1045-9.

[17] L. Chaunier, G. Della Valle, D. Lourdin, A.L. Réguerre, K. Cochet, E. Leroy, Viscous sintering kinetics of biopolymer filaments extruded for 3D printing, Polym Test. 77 (2019) 105873. https://doi.org/10.1016/j.polymertesting.2019.04.020.

[18] L. Chaunier, A.L. Réguerre, E. Leroy, Contour fitting of fused filaments cross-section images by lemniscates of booth: Application to viscous sintering kinetics modeling, Polymers (Basel). 13 (2021). https://doi.org/10.3390/polym13223965.

[19] B. Zhang, A. Gleadall, P. Belton, T. Mcdonagh, R. Bibb, S. Qi, New insights into the effects of porosity, pore length, pore shape and pore alignment on drug release from extrusionbased additive manufactured pharmaceuticals, Addit Manuf. 46 (2021). https://doi.org/10.1016/j.addma.2021.102196.

[20] L. Chaunier, L. Viau, X. Falourd, D. Lourdin, E. Leroy, A drug delivery system obtained by hot-melt processing of zein plasticized by a pharmaceutically active ionic liquid, J Mater Chem B. 8 (2020) 4672–4679. https://doi.org/10.1039/d0tb00326c.

[21] J.L. Shamshina, Chemistry: Develop ionic liquid drugs, Nature. 528 (2015) 188–9. https://doi.org/10.1038/528188a.

[22] M. Thadasack, L. Chaunier, H. Rabesona, L. Viau, M. De-Carvalho, G. Bouchaud, D. Lourdin, Release kinetics of [lidocainium][ibuprofenate] as Active Pharmaceutical Ingredient-Ionic Liquid from a plasticized zein matrix in simulated digestion, Int J Pharm. 629 (2022). https://doi.org/10.1016/j.ijpharm.2022.122349.

[23] J. Villanova, R. Daudin, P. Lhuissier, D. Jauffrès, S. Lou, C.L. Martin, S. Labouré, R. Tucoulou, G. Martínez-Criado, L. Salvo, Fast in situ 3D nanoimaging: a new tool for dynamic characterization in materials science, Materials Today. 20 (2017) 354–359. https://doi.org/10.1016/j.mattod.2017.06.001.

[24] A.K. Schomberg, A. Diener, I. Wünsch, J.H. Finke, A. Kwade, The use of X-ray microtomography to investigate the microstructure of pharmaceutical tablets: Potentials and comparison to common physical methods, Int J Pharm X. 3 (2021). https://doi.org/10.1016/j.ijpx.2021.100090.

[25] E. Olăreț, I.C. Stancu, H. Iovu, A. Serafim, Computed tomography as a characterization tool for engineered scaffolds with biomedical applications, Materials. 14 (2021). https://doi.org/10.3390/ma14226763.

[26] A.I. Kondarage, G. Poologasundarampillai, A. Nommeots-Nomm, P.D. Lee, T.D. Lalitharatne, N.D. Nanayakkara, J.R. Jones, A. Karunaratne, In situ 4D tomography image analysis framework to follow sintering within 3D-printed glass scaffolds, Journal of the American Ceramic Society. 105 (2022) 1671–1684. https://doi.org/10.1111/jace.18182.

[27] A. Nommeots-Nomm, C. Ligorio, A.J. Bodey, B. Cai, J.R. Jones, P.D. Lee, G. Poologasundarampillai, Four-dimensional imaging and quantification of viscous flow sintering within a 3D printed bioactive glass scaffold using synchrotron X-ray tomography, Mater Today Adv. 2 (2019). https://doi.org/10.1016/j.mtadv.2019.100011.

[28] F. García-Moreno, P.H. Kamm, T.R. Neu, F. Bülk, M.A. Noack, M. Wegener, N. von der Eltz, C.M. Schlepütz, M. Stampanoni, J. Banhart, Tomoscopy: Time-Resolved Tomography for Dynamic Processes in Materials, Advanced Materials. 33 (2021). https://doi.org/10.1002/adma.202104659.

[29] C. Jouannin, C. Tourné-Péteilh, V. Darcos, T. Sharkawi, J.M. Devoisselle, P. Gaveau, P. Dieudonné, A. Vioux, L. Viau, Drug delivery systems based on pharmaceutically active ionic liquids and biocompatible poly(lactic acid), J Mater Chem B. 2 (2014) 3133–3141. https://doi.org/10.1039/c4tb00264d.

[30] P. Decaen, A. Rolland-Sabaté, G. Colomines, S. Guilois, D. Lourdin, G. Della Valle, E. Leroy, Influence of ionic plasticizers on the processing and viscosity of starch melts, Carbohydr Polym. 230 (2020). https://doi.org/10.1016/j.carbpol.2019.115591.

[31] Y. Son, Determination of shear viscosity and shear rate from pressure drop and flow rate relationship in a rectangular channel, Polymer (Guildf). 48 (2007) 632–637. https://doi.org/10.1016/j.polymer.2006.11.048.

[32] T. Weitkamp, M. Scheel, J. Perrin, G. Daniel, A. King, L. Roux, V., J.-L. Giorgetta, A. Carcy, F. Langlois, K. Desjardins, C. Menneglier, M. Cerato, C. Engblom, G. Cauchon, T. Moreno, C. Rivard, Y. Gohon, F. Polack, Microtomography on the ANATOMIX beamline at Synchrotron SOLEIL, (2022). https://doi.org/10.1088/1742-6596/2380/1/012122.

[33] T. Weitkamp, M. Scheel, J.L. Giorgetta, V. Joyet, V. Le Roux, G. Cauchon, T. Moreno, F. Polack, A. Thompson, J.P. Samama, The tomography beamline ANATOMIX at Synchrotron SOLEIL, in: J Phys Conf Ser, Institute of Physics Publishing, 2017. https://doi.org/10.1088/1742-6596/849/1/012037.

[34] K. Desjardins, M. Scheel, J.-L. Giorgetta, T. Weitkamp, C. Menneglier, A. Carcy, Design of Indirect X-Ray Detectors for Tomography on the Anatomix Beamline; Design of Indirect X-

Ray Detectors for Tomography on the Anatomix Beamline, (2018). https://doi.org/10.18429/JACoW-MEDSI2018-THPH09.

[35] A. King, N. Guignot, P. Zerbino, E. Boulard, K. Desjardins, M. Bordessoule, N. Leclerq, S. Le, G. Renaud, M. Cerato, M. Bornert, N. Lenoir, S. Delzon, J.P. Perrillat, Y. Legodec, J.P. Itié, Tomography and imaging at the PSICHE beam line of the SOLEIL synchrotron, Review of Scientific Instruments. 87 (2016). https://doi.org/10.1063/1.4961365.

[36] A. Mirone, E. Brun, E. Gouillart, P. Tafforeau, J. Kieffer, The PyHST2 hybrid distributed code for high speed tomographic reconstruction with iterative reconstruction and a priori knowledge capabilities, Nucl Instrum Methods Phys Res B. 324 (2014) 41–48. https://doi.org/10.1016/j.nimb.2013.09.030.

[37] R.W. Hopper, Coalescence of Two Equal Cylinders: Exact Results for Creeping Viscous Plane Flow Driven by Capillarity, Journal of the American Ceramic Society. 67 (1984) C-262-C-264. https://doi.org/10.1111/j.1151-2916.1984.tb19692.x.

[38] S.G. Giteru, M.A. Ali, I. Oey, Recent progress in understanding fundamental interactions and applications of zein, Food Hydrocoll. 120 (2021) 106948. https://doi.org/10.1016/j.foodhyd.2021.106948.